CHAPTER 3:
THE STAR SILICON DRIFT DETECTOR

3.1 The STAR Silicon Vertex Tracker (SVT)

3.1.1 Overview of the STAR experiment at RHIC

The primary goals of High-Energy Heavy-Ion Physics is to investigate the behavior of hadronic and nuclear matter at extreme conditions of temperature and density (ε > 1-2 GeV/fm^3) [ref. 3.1]. Specific motivation from Quantum Chromodynamics (QCD) is given by the possibility to create macroscopic volumes of nuclear matter at such extreme thermodynamic conditions that the forces which confine the constituents in normal hadrons can be overcome, resulting in a phase transition to a new form of matter known as Quark Gluon Plasma (QGP) [ref. 3.2, 3.3]. QCD lattice calculations [ref. 3.4] predict a phase transition from hadronic matter to a QGP at a temperature near 2.3×10^{12} *K* (*200 MeV*). Such a state is believed to have existed shortly after the Big Bang (around *200 ms*), and may still exist in the core of dense stars. The Relativistic Heavy Ion Collider (RHIC) is being constructed at Brookhaven National Laboratory to create this new state of matter and investigate its fundamental properties. At RHIC Gold (Au) beams will be accelerated and collide at incident energies up to *100 + 100 GeV* per nucleon. This energy is estimated to be sufficient to provide the necessary conditions for the formation of the QGP.

The STAR experiment (Solenoidal Tracker at RHIC) is one of two major experiments that are under construction for RHIC [ref. 3.5]. The STAR experiment

will search for signatures of QGP formation and investigate the behavior of strongly interacting matter at high densities. Since no single definitive signature for the formation of QGP has been found yet, it is important to use a flexible detection system that allows the correlation of the different observable parameters and possible signatures. The STAR detector system will concentrate on measurements of hadron production over a large solid angle and will be capable of studying the reaction observables such as temperature, flavor composition, collision geometry, energy density fluctuation and particle production on an event-by-event basis.

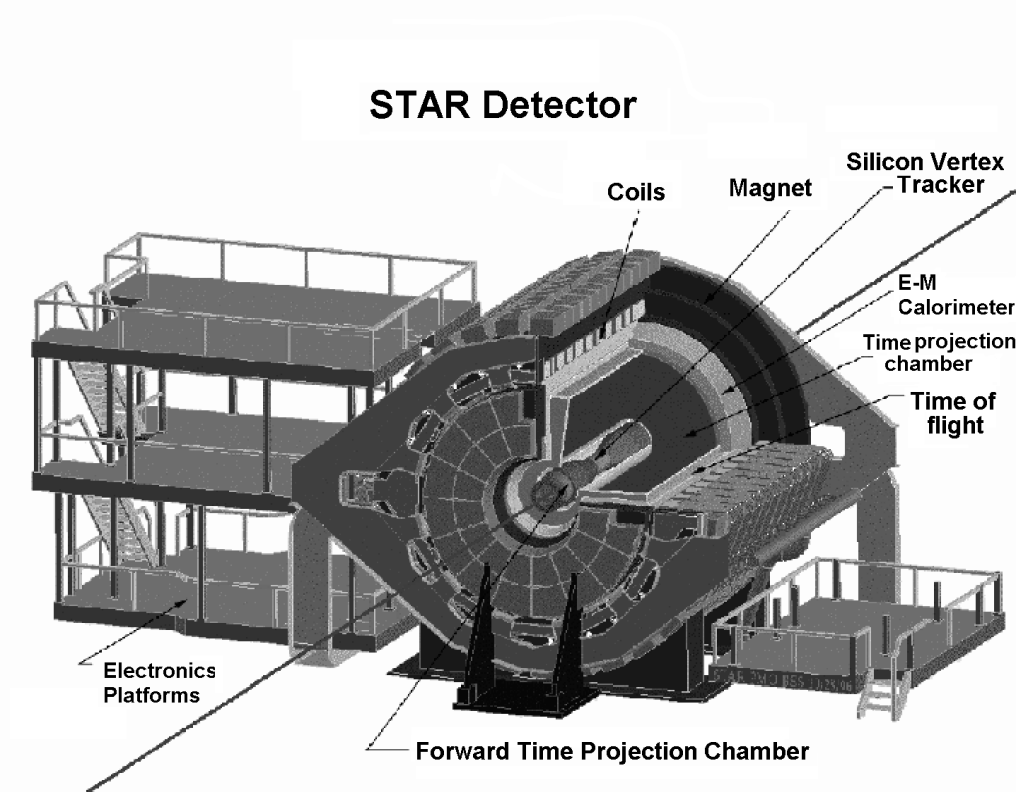

Figure 3.1: *Schematic layout of the Solenoidal Tracker At RHIC (STAR).*

The configuration of the STAR detector is shown in figure 3.1. Its main detector components are a Time Projection Chamber (TPC), the Silicon Vertex Tracker (SVT), an Electromagnetic Calorimeter (EMC) and trigger counters.

These detectors are assembled in a large room temperature solenoidal magnet that will provide a *0.5 Tesla* magnetic field. The TPC detector will track and measure charged particles around mid-rapidity ($|\eta| \leq 2$) with full azimuthal coverage. With the TPC alone, STAR is limited to the study of hadrons with a transverse momentum (p_T) above *150 MeV/c* due to the sweep of the applied magnetic field, and it has a modest efficiency and accuracy for the study of short lived particles that decay before the TPC. Multi-strange baryons and anti-baryons cannot be studied with the TPC only.

3.1.2 The Silicon Vertex Tracker (SVT)

The SVT will enhance the overall performance of STAR by extending the particle tracking to a position closer to the primary vertex thus improving the momentum resolution and the momentum range. It will store three dimensional space points and the resulting tracking vectors will be matched with the TPC tracks. It is designed to determine the position of the primary vertex to an accuracy better than 100 μm. In addition, due to its proximity to the primary vertex, it enables the reconstruction of secondary vertices from short-lived hadronic particles (K_s^0, ϕ, Λ, $\overline{\Lambda}$, Ξ^-, Ω^-) that decay before the TPC.

The SVT consists of 216 Silicon drift detectors mounted on three concentric barrels. Figure 3.2 shows a schematic drawing of the SVT layout. The detectors are overlapped in azimuthal direction to minimize non-active areas. The wafers are mounted onto Beryllium ladder structures holding 4, 6 or 7 detectors depending on the barrel number. The ladders are arranged in a shape of polygon barrels with 8, 12 and 16 ladders each to encompass the colliding beams and their point of interaction at radii of 6.6, 10.6 and 14.5 cm respectively. It will provide full azimuthal coverage and span a pseudo-rapidity range of $-1 \leq \eta \leq 1$. Table 3.1 summarizes some of the SVT specifications.

Table 3.1: Design specifications of the STAR/SVT	
Length of active area: Inner barrel Middle barrel Outer barrel	 25.2 cm 37.8 cm 44.1 cm
Pseudo-rapidity coverage:	$-1 \leq \eta \leq +1$
Radial distance: Inner barrel Middle barrel Outer barrel	 6.6 cm 10.6 cm 14.5 cm
Total number of detector wafers: Inner barrel Middle barrel Outer barrel	216 32 (8 × 4) 72 (12 × 6) 112 (16 × 7)
Total number of wafers including spares:	250
Thickness of each detector wafer Total thickness	300 μm 900 μm ~ 0.9% X_0
Average Radiation length, (total, including electronics)	4.5%

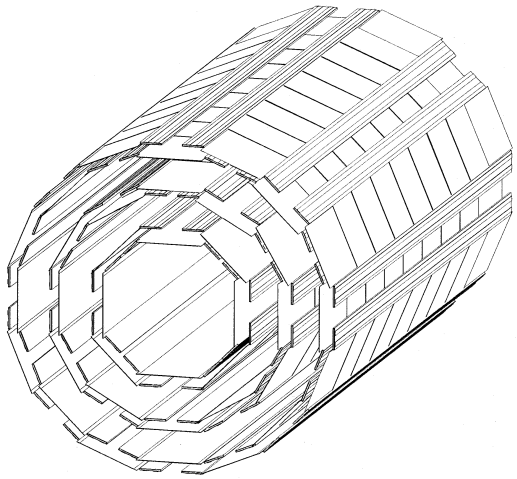

Figure 3.2: *The Silicon Vertex Tracker (SVT) layout.*

On each individual ladder, schematically shown in figure 3.3, the detectors will be assembled side by side in such a way that the cathode voltages can be daisy-chained from detector to detector, therefore, minimizing the number of HV cables. The anodes are connected to the input channels of the pre-amplifiers (PASA) through wire bonds. The PASA together with another integrated chip, the

SCA (Switched Capacitor Array) is part of the front-end electronics multi-chip module (HYBRID). The short distance between the anodes and the front-end electronics was designed to keep the input capacitance low, and consequently, keep the electronic noise level low.

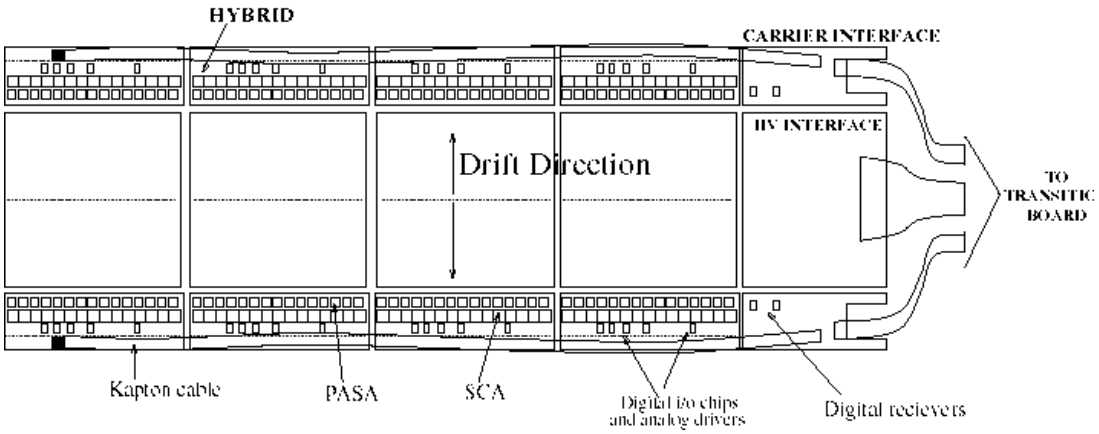

Figure 3.3: *Schematic drawing of a ladder. Each component of the ladder will be described in further sections of this thesis.*

The support structure that will hold the ladders in their honeycomb structured super-layer position is made of Beryllium. It has a low interaction length minimizing the production of secondary particles as well as the effects of multiple Coulomb scattering on the traversing particles. Further design specifications can be found in reference 3.6.

3.1.3 Main requirements for Silicon Drift Detectors in STAR

The Silicon Drift Detectors for the SVT must satisfy a number of requirements based on the physics goals and the specific collider environment. Some of these requirements are:

- **Maximum coverage with a minimum dead area.** The Silicon wafers will be mounted in three concentric barrels with each barrel composed of several

wafers mounted on a ladder configuration. Dead area caused by the anodes and the front-end-electronics can be eliminated by overlapping the adjacent ladders, but the dead area between detector wafers on the same ladder cannot be avoided. In the final design, the detector dimensions are $6.3 \times 6.3\ cm^2$. The dead area of the detector is basically given by the high voltage guard area, which has been optimized to *6.4 %* of the total detector area.

- **High position resolution.** The SVT is the inner-tracking detector of STAR, and it will be placed near the reaction point. We expect around 2000 charged particles to traverse the detectors for each central Au+Au collision, therefore the detector needs to have excellent position resolution in order to permit accurate tracking and vertexing. As will be discussed later, the position resolution is strongly dependent on good drift linearity. Voltage non-linearity and localized lattice non-uniformities are some of the factors that can affect the position resolution.

- **Low radiation length.** The SVT should introduce as little material as possible into the tracking region to minimize multiple Coulomb scattering of the traversing particles. This also reduces the creation of secondaries such as δ-electrons and X-rays.

- **Radiation hardness.** The Silicon wafers and front-end-electronics should be sufficiently hard to withstand 10 years of RHIC operation (1 year ≈ 1 Krad).

3.2 Brief history of the detector design development

The first STAR Silicon drift detector prototype, STAR-1, was designed and developed on a *75 mm* diameter NTD type Silicon wafer (described later in section 3.3.1.3 and in references 3.7 and 3.8). The material had a resistivity of

approximately *3.0 kΩ·cm*. Figure 3.4(a) shows a schematic layout of the detector, which was designed as a one-directional drift detector. The detector size was *4.5 × 4.5 cm*^{2}, the maximum drift distance was *4.0 cm*, with 179 anodes distributed on one side of the detector. The anodes were *200 × 200 μm* in size with a spacing of *250 μm*. The drift field was defined by parallel cathode strips oriented perpendicular to the drift direction with a pitch of *120 μm*. Up to *2500 V* was applied in the highest cathode strip to obtain a reasonable drift time. A significant guard area was required to support such high biases. In this design, *22%* of the total area was inactive due to the guard structure.

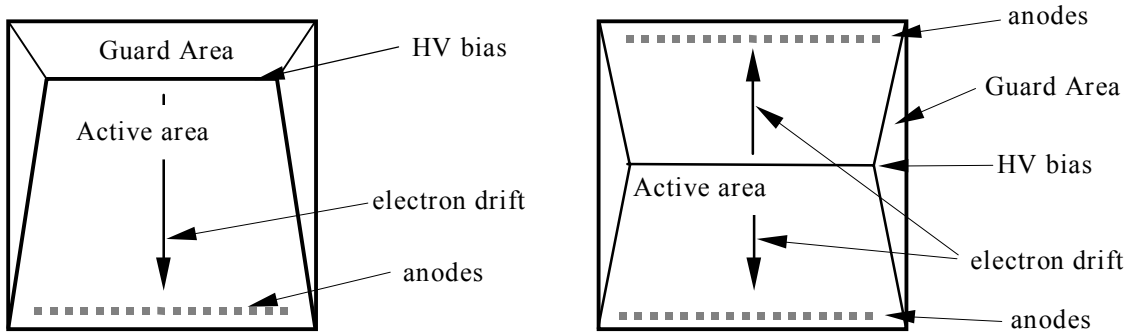

(a) STAR-1 design **(b) STAR-2 design**

Figure 3.4: *Geometrical layout of the STAR-1 (a) and STAR-2.0 (b) detector.*

The STAR-2.0 detector design was changed to have two separate drift areas, with opposite drift directions, as shown in figure 3.4(b). By using a *100 mm* diameter wafer, the detector size was increased to *6 × 6 cm*^{2} and the maximum drift distance was reduced to *3 cm*. With a shorter drift distance, less high voltage, namely *1500V*, was required to accomplish the same drift time than for the STAR-1 detector and consequently the size of the guard area was reduced. In the STAR-2.0 design, the inactive guard area accounts for only 5% of the total area.

Four variations of the STAR-2.0 detector, testing different designs of the HV guard area were produced. Two types of guard lines structure were proposed: a

chevron type and connecting lines. Also, the guard lines were of two types, either implanted lines with an Aluminum overlay or lines with only the Aluminum overlay (field plate lines). From the four variations of the STAR-2.0 detector, only the design with the connecting guard lines of field plate type has shown to perform satisfactory, and was therefore used for the next prototype, STAR-2.5. For more details on the guard area design variations, see reference 3.9.

From STAR-2.0 to STAR-2.5, a few processing steps were changed. Mainly the oxide step-cut of the processing procedure was modified to reduce the amount of the photolithography masks. The key processing steps for the STAR detectors are described in reference 3.10 and 3.11.

Results from the STAR-2.5 batch were not as good as expected. A production yield of 50% was achieved, but most of the detectors performed below expectation. Voltage breakdowns and high leakage current were measured. Also, instability of the anode leakage current showed how sensitive the detectors were to external conditions such as temperature and humidity. However, it was shown that the simplification in the detector processing steps had improved the production yield and had not affected the detector quality.

Due to the high voltage breakdown problems of the STAR-2.5 prototype the design of the implanted resistors was changed and the resistance value was increased from *650 kΩ* to *1 MΩ*. In addition, the cathode pitch was increased from *120 μm* to *135 μm*. The whole detector was stretched to $6.3 \times 6.3\ cm^2$ to take full advantage of the *100 mm diameter* Silicon wafer. The shape of the guard structure was changed to yield the maximum active area. One final addition to the STAR-2.7 detector was the polyamide coating to protect the detectors from humidity.

The STAR-2.7 prototype was the first design to be sent out and produced by a commercial company. STAR-2.7 detectors were produced in parallel by the Instrumentation Division at Brookhaven National Laboratory and SINTEF, a

Norwegian semiconductor company. These detectors were tested intensively, and with the higher number of detectors produced, it was possible to study in detail each feature of the detector. Some results from the STAR-2.7 detectors are shown in the following chapters.

In the new STAR-2.9 design, the guard area was slightly increased to better distribute the voltage drop. The total active area of the detector was reduced from 96% to 94.5%, however the increase of the guard area improved considerably the voltage linearity and reduced the anode leakage current which resulted in a more reliable detector. To further improve the voltage linearity, the implanted resistor value was lowered from *1 MΩ* to *0.5 MΩ*, a lower resistor enhances the stiffness of the resistor chain, thus reducing the voltage non-linearities due to leakage currents.

Another major improvement from the STAR-2.7 to the STAR-2.9 design is achieved by optimizing the design of the focusing electrodes: E1, W1. Detectors from the STAR-2.7 batch had shown to be very sensitive to voltage variations on the focusing electrodes. Also, there was a large non-uniformity in the charge collection between anodes in the same detector. The modifications made for the STAR-2.9 batch had increased the focusing voltage bands and improved the uniformity of anode charge collection. Details of these measurements and the modifications made are discussed in Chapter 3.

Other minor additional changes that were made between the STAR-2.7 and STAR-2.9 designs, include the position of the charge injection lines and the widening of the Aluminum overlay of the cathodes. There was an intermediate version, STAR-2.8, that already used most of the features of the final STAR-2.9 design. However, due to a design problem in the guard area, those detectors had a very low yield.

Further details of the earlier prototypes can be found in references 3.9, 3.12 and 3.13. This thesis will concentrate on the results from prototype batch STAR-2.7 and the operational properties of the final detector version, STAR-2.9.

The table below shows a summary of the different types of detector design produced during the development phase of the STAR/SVT Silicon drift detector project, previous to the final detector design.

Detector Prototype	Year	Produced by:	Quantity produced	Production yield
STAR-1	1992	BNL	10	40%
STAR-2.0	1993	BNL	12	30%
STAR-2.5	1994	BNL	8	50%
STAR-2.7	1995	BNL	24	60%
STAR-2.7	1996	SINTEF	32	60%
STAR-2.8	1996-1997	BNL	8	40%
STAR-2.9	1997	BNL+SINTEF	50	70%
STAR-2.9	1998	BNL +SINTEF	250 (expected)	70% (expected)
STAR-2.9	1999	BNL+SINTEF	350 (expected)	70% (expected)

3.3 Details of the STAR/SVT Silicon Drift Detector final design

The STAR/SVT Silicon drift detector is produced using a *100 mm* diameter, *280 μm* thick, neutron transmutation doped type (NTD, see section 3.3.1.3) Silicon wafer with an approximate resistivity of *3.0 kΩ·cm*. Figure 3.5 shows a schematic layout of the STAR drift detector. The detector is divided in two symmetrical parts that correspond to the two drift areas, top and bottom. The active area (drift region) of the detector is covered with p+ implant cathode electrodes that will generate the drift field necessary to move the electron cloud towards the anode region. The p+ implant strips are on both surfaces of the detector, p-side and n-

side. On the n-side surface, in both parts, top and bottom, there are 240 n+ implant anodes aligned at the edge of the detector with a spacing of *250 μm*.

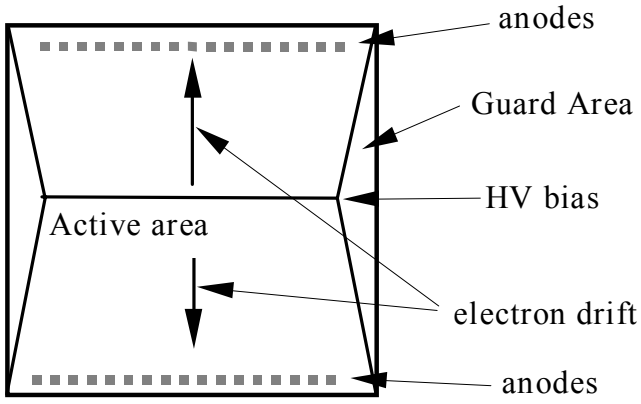

Figure 3.5: *Schematic layout of the Silicon drift detector.*

The cathodes are biased negatively with respect to the anodes thus creating a constant electric field that will force the electrons to drift towards the anodes. Close to the anodes, special electrodes, called focusing electrodes will shape the potential distribution in such a way that the electrons will drift into the anodes.

On the lateral sides of the detector there is a small guard region to reduce the potential at the edge of the detector down to zero. Guard lines are connected to every 10 cathodes connecting equivalent cathodes of the top part to the bottom part. This way, each guard line is biased by the cathodes. The guard region constitutes an inactive part of the detector, and therefore has to be designed to be as small as possible.

In the following sections, each of the different regions of the detector will be described in detail. For reference purpose, some numbers and dimensions can also be found in Appendix C.

3.3.1 The drift region

The drift region is the active part of the detector. In its final design, this region is divided into two symmetric parts as shown in figure 3.4. With a two-directional drift detector, the maximum drift distance is lower, therefore it requires a lower bias value which allows the reduction of the detector guard area. Each half of the detector is composed of 221 parallel cathode strips on both surfaces of the detector, oriented perpendicular to the drift direction. Each cathode strip is *100 μm* wide spaced by a pitch of *135 μm* from cathode to cathode. A section of the detector design is detailed in figure 3.6.

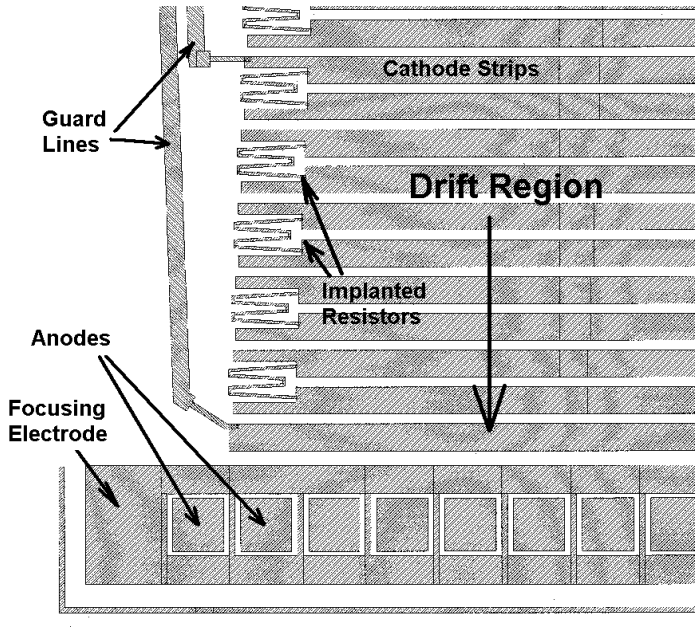

Figure 3.6: *Schematic view of a section of the detector.*

The cathodes are numbered from 0 to 221, where cathode number "0" is the cathode strip closest to the anodes and cathode 221 is the center cathode that will be biased with the highest negative voltage. The cathodes on the n-side surface are named "n0" to "n221" and the cathodes on the opposite surface are named "p0" to "p221".

The cathodes are biased to generate a potential electric field that has two major functions: to deplete the detector bulk from free electrons and to generate a constant electric field to drift the signal electrons to the anodes. Each cathode strip constitutes a p-n diode junction, and by reverse biasing the diode, the Silicon bulk is depleted of its free electrons (see Chapter 1.3.3). Both sides of the detector are biased sufficiently high to fully deplete the detector bulk. The potential distribution can be calculated by solving the Poisson equation, which yields a parabolic shape with a potential minimum in the center of the detector.

To generate the drift field, the 221 cathodes are connected in series through implanted resistors forming a voltage divider that will gradually decrease the voltage from cathode to cathode. In the final SVT configuration, the center cathode will be biased at a maximum voltage of $-1500V$ ($500V/cm$), which is sufficient to fully deplete the detector bulk and generate a reasonable drift velocity of approximately $6.5\ \mu m/ns$.

Electrons generated during the passage of an ionizing particle will first be transported towards the center plane of the detector by the parabolic component of the electric field in the transverse direction of the detector, and then they will be transported towards the anode by the linear component in the drift direction. Details of the electric field calculation are shown in the following section.

3.3.1.1 Potential distribution in the drift region

As described in chapter 2, the depletion thickness underneath a $p+$ cathode varies with the applied reverse bias as:

$$W = \sqrt{\frac{2\varepsilon V}{qN_D}} \tag{3.1}$$

where N_D is the bulk donor concentration and ε is the permittivity of the material. In the case of the SVT Silicon drift detectors, a double-sided detector, the bulk is fully depleted when the sum of the depletion thickness from both sides is higher than the bulk thickness, *280 μm*. Solving equation 3.1 for a *3.0 kΩ·cm* Silicon wafer shows that *23 V* on both side of the detector is sufficient to fully deplete the detector bulk.

Once the detector bulk is fully depleted, the potential distribution is determined by solving the Poisson equation:

$$\frac{d^2}{dy^2}\varphi + \frac{d^2}{dz^2}\varphi = -\frac{\rho}{\varepsilon} \tag{3.2}$$

where $\rho = eN_D$ is the charge density of the ionized donor, 'z' is the direction across the detector from surface to surface and 'y' is the drift direction. By using the variable separation method, the solution can be written as a series:

$$\varphi(y,z) = -E_{drift}\, y - \frac{eN_D}{2\varepsilon} z^2 + \sum_{n=1}^{\infty}\left(A_n \sin\frac{2\pi n}{L} y + B_n \cos\frac{2\pi n}{L} y \right)\cosh\frac{2\pi n}{L} z \tag{3.3}$$

where *z=0* denotes the middle of the bulk and *L* is the cathode pitch. The first term in the equation corresponds to the linear term representing the homogeneous drift field in the 'y' direction. This term causes the electron cloud to drift in the 'y' direction, parallel to the detector surface, at a constant speed towards the anodes. The second term in the equation represents the parabolic Coulomb potential

component in the 'z' direction. This term confines the electrons to the middle of the detector bulk. The depth of the potential valley is given by:

$$\Delta V = \frac{eN_D}{2\varepsilon_{Si}}\left(\frac{d}{2}\right)^2 \qquad \textbf{(3.4)}$$

where $d=280\ \mu m$ which corresponds to the detector thickness. For $3.0\ k\Omega{\cdot}cm$ Silicon, the depth of the potential valley is approximately $\Delta V=23V$. The third term of equation 3.3 corresponds to the potential deviations from an ideal case caused by the discrete nature of the potential distribution near the surface, due to the finite size of the cathodes. The magnitude of these variations decays exponentially with distance from the surface towards the bulk center. Also near the surface, between the cathode strips, fixed positive charges in the Si-SiO_2 interface create a potential perturbation that is not included in equation 3.3. This effect related to surface charge injection will be discussed in detail in the following chapter.

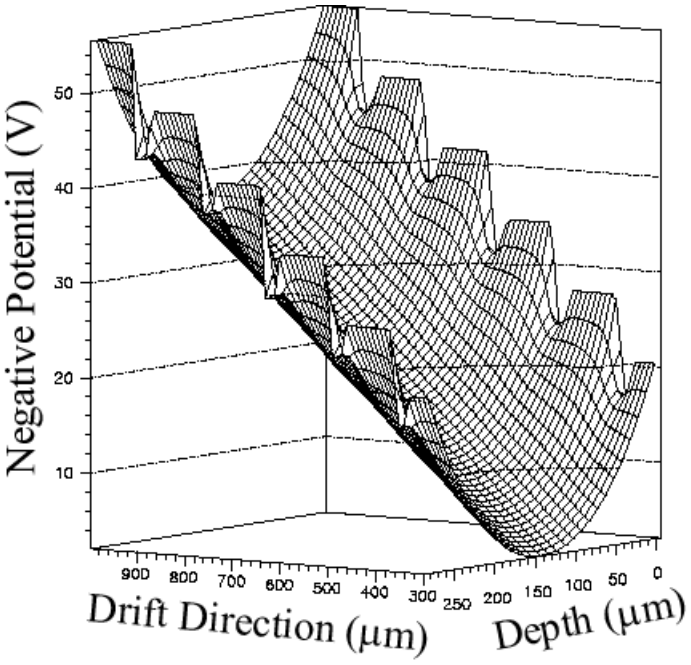

Figure 3.7: *Potential distribution in the drift region.*

Figure 3.7 shows a 2-dimensional map of the resulting potential distribution in the depleted Silicon. This distribution was calculated with a simulation package [ref. 3.14] that takes into account the known bulk quantities such as doping density, dielectric constant and also the boundary conditions such as applied potentials. For illustrative purposes, the quantity plotted corresponds to the negative potential.

3.3.1.2 The internal and external voltage divider

The internal voltage divider is composed of implanted resistors that connect the cathodes in series, thus reducing the potential gradually from the high voltage region down to the anode region. These implanted resistors are basically p+ implantation with the same sheet resistance than the cathodes but with a different geometry. The resistance of an implanted structure is determined by:

$$R = \rho \frac{\ell}{A} \tag{3.5}$$

where ρ is the sheet resistance, "ℓ" is the length of the resistor and "A" is the cross section area of the implanted volume. Figure 3.7 shows two implanted resistor designs that were used and tested in the STAR/SVT drift detectors. The cross section area "A" of the resistor is small compared to the cathode area, therefore, most of the voltage drop occurs in the resistor and the potential along the cathode can be considered constant. The first design shown in figure 3.8a was used in earlier detector prototypes [ref. 3.9] but it could not sustain high voltage differences. The second and final resistor design, depicted in figure 3.8(b) has been used in all later detector prototypes.

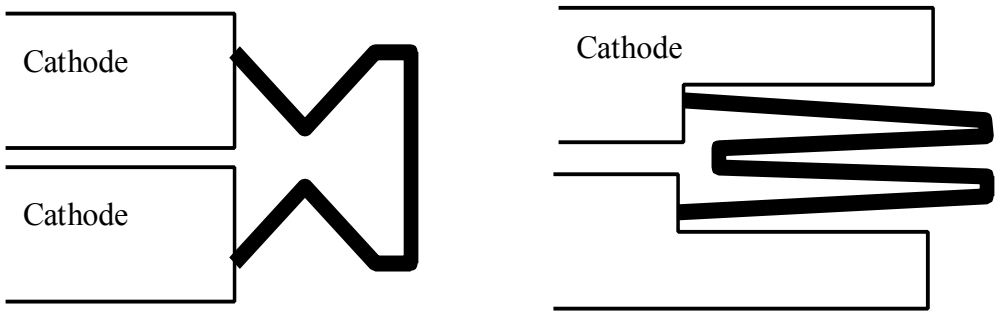

Figure 3.8: *Two different design of the implanted resistor. The first one (a) was used on prototypes STAR-1 to STAR-2.5. The second (b), "W" shaped design is the final design, used in the prototypes from STAR-2.7.*

Implanted resistors are an undesirable source of heat, therefore, the values of the resistance must be chosen with some consideration. If the resistor value is too low, there will be too much heat dissipation. On the other hand, if the resistor value is too high, the total current through the resistor chain becomes too low and susceptible to surface leakage currents. In the STAR detector prototypes, the implanted resistor values have varied from *500 kΩ* to *1.0 MΩ*. These values were chosen empirically based on previous experiences. In a detector implemented with *500 kΩ* resistors, the total current through the resistor chain is on the order of *15 μA*, which is an order of magnitude higher than the expected total leakage current through the cathode surface.

Ideally, one would like to bias only the highest cathode strip and have the implanted voltage divider uniformly reduce the voltage down to zero, thus creating a constant electric field. However, leakage currents from the cathode strips to ground through paths other than the resistor chain change the voltage distribution. Figure 3.9 shows an example of voltage distributions measured in two different detector prototypes. The first pair of curves, represented by open squares is from a detector with very low leakage currents. The second pair of curves, represented by the solid circles is from a detector with high leakage currents. Most of the leakage

current is escaping through the guard area on the side of the detector. In addition, thermally generated electron-hole pairs at the *Si-SiO₂* interface can also contribute to the total leakage current. Detectors with a "bad" *Si-SiO₂* interface can have a considerable amount of leakage current.

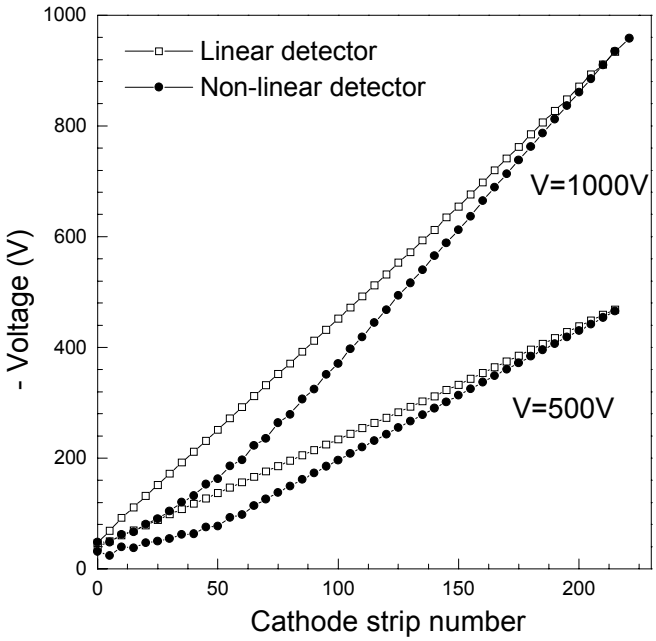

Figure 3.9*: *Example of a linear and a non-linear bias distribution of the cathodes measured from STAR-2.7 prototype detectors.

Considering that each cathode strip leaks the same amount "*i*" of leakage current, for a certain cathode strip "*k*", the current can be written by:

$$I(k) = I_0 + k \cdot i \qquad \textbf{(3.6)}$$

where I_0 is the remaining current at the end of the resistor chain at the last cathode strip. Then the potential of cathode strip "*k*" can be calculated as:

$$V(k) = \sum_{n=0}^{k} R_n \cdot I(k) = R \cdot \sum_{n=0}^{k} (I_0 + n \cdot k) = R \cdot \left(k \cdot I_0 + \frac{k(k+1)}{2} \right) \quad \textbf{(3.7)}$$

Which gives a quadratic dependence of the voltage distribution:

$$V(k) = V_0 \cdot k + \Delta V \cdot k^2 \quad \textbf{(3.8)}$$

As seen in figure 3.9. To solve this problem, an external voltage divider with a much lower resistance is used to maintain the voltage linearity. Every 10th cathode strip is connected through a wire bond to this external voltage divider that has a total resistance on the order of 100 times smaller than the internal divider.

3.3.1.3 Bulk doping

The STAR/SVT Silicon drift detector is fabricated using a n-type material as the substrate. In this case, the reverse bias condition of the cathode p-n junction requires the applied potential to be negative. Therefore, the electrons drift inside the Silicon and are collected in the anodes to generate the output signal. In principle, a drift detector fabricated on a p-type material can operate under the same concept, with positive voltage applied to the cathodes and the holes drifting towards the anodes instead of electrons. However, the mobility constant of the electrons in Silicon is slightly higher than the mobility of the holes, therefore, a faster drift velocity is achievable with the n-type substrate. P-type Silicon drift detectors have been tried and some results can be found in ref. 3.15.

The homogeneity of bulk doping is an important factor for the drift uniformity. Standard Silicon crystal growing techniques are used more commonly for p-type crystals. N-type crystals are more difficult to grow due to the fact that the Phosphorous used as impurity in n-type materials has a small diffusion

coefficient with respect to the Silicon. For that reason, the Phosphorous concentration in the Silicon crystal is strongly dependent on the temperature which makes it difficult to achieve a uniform distribution. On the other hand, the Boron (acceptor) diffusion coefficient is significantly closer to that of the Silicon, therefore it diffuses much easier and more uniformly in the Silicon crystals. For that reason, the Boron implantation is less susceptible to temperature variation and high levels of homogeneity are achievable.

The way to produce high-homogeneity n-type semiconductor materials is by a process called Neutron Transmutation Doping (NTD) [ref. 3.7, 3.8]. In this process, impurity isotopes are created from the atoms of the crystal lattice by thermal-neutron irradiation and subsequent radioactive decay. For Silicon, the NTD process is represented by the equation below.

$$Si^{30} + n \rightarrow Si^{31} + \gamma$$
$$Si^{31} \rightarrow P^{31} + e^{-} \qquad \textbf{(3.9)}$$

Si^{30} nucleus turns into Si^{31} by capturing a thermal neutron and emitting a γ photon. Subsequently, the Si^{31} with a half-life of 2.62 hours decays by β emission to the stable isotope P^{31}. However, the Silicon crystal has a natural abundance of only 3.10% of Si^{30} isotope. The most common isotope is the Si^{28} with 92.29% and secondly the Si^{29} isotope with 4.67%. These two isotopes undergo the following reactions:

$$Si^{28} + n \rightarrow Si^{29} + \gamma$$
$$Si^{29} + n \rightarrow Si^{30} + \gamma \qquad \textbf{(3.10)}$$

Fast neutrons can also induce the following reactions:

$$Si^{28} + n \rightarrow Mg^{25} + \alpha$$
$$Si^{29} + n \rightarrow Mg^{26} + \alpha \quad \textbf{(3.11)}$$

To produce the n-type Silicon with the NTD process, a p-type high resistivity (*~20 kΩ·cm*) Silicon is used. If the concentration of created donor atoms is much higher than the initial acceptor concentration, the final doping homogeneity will only depend on the spatial homogeneity of the neutron beam. Typical neutron beam homogeneity is around 2 to 3%.

During the neutron radiation, other undesirable effects can take place as well. A γ flux, proportional to the neutron flux increases the temperature of the Silicon wafer requiring the Silicon to be cooled during the irradiation process. But probably the most undesirable effect is the radiation damage in the Silicon lattice caused by fast neutrons. A Silicon atom can be displaced from its normal lattice position creating a vacancy that acts as a deep acceptor, thereby affecting the properties of the material. Typically, for each new Phosphorous atom created by the NTD process, many more effective acceptors are created by radiation damage. Therefore, after the irradiation, the Silicon still tends to be a p-type semiconductor. In order to reverse the material, the Silicon crystal has to subsequently undergo an annealing process, during which the wafer is kept at high temperature (*800°C*) for a certain period of time (~1 hr).

3.3.1.4 The cathode Aluminum overlay

At the edge of the cathodes, where the *p+* implant ends and the SiO_2 starts, the accumulated charge under the SiO_2 creates a high electric field. This can cause an avalanche breakdown of the bias at that point, which increases the generated leakage current. To lower this junction electric field, the cathode Aluminum is spread beyond the implantation limits over the oxide layer, as shown in figure

3.10. With this field-plate overlay, the maximum electric field is reduced and shifted from the edge of the p-n junction up to the end of the field-plate. In the final design of the STAR detector, the cathode Aluminum overlay is approximately *20 μm* wider than the cathode implantation.

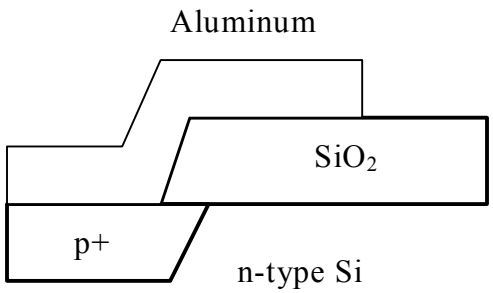

Figure 3.10: *Edge of the cathode with the Aluminum overlay.*

3.3.2 Charge injection calibration lines

The drift velocity in the Silicon is dependent on the temperature. To achieve the high position resolution expected for the SVT, a drift velocity calibration is required. The drift velocity calibration is accomplished by injecting charge at known drift distances across the detector. For that purpose, the detector is instrumented with 8 injection lines on the n-side surface of the detector. They are placed at distances of *0.2 cm*, *1.0 cm*, *2.0 cm* and *3.0 cm* from the anodes in both drift directions. The injection lines are pulsed with an AC pulse that will inject charge from the surface of the detector into the bulk. The injected charge will drift following the same path as the charge generated by a particle.

Several different ways of charge injection are possible [ref. 3.16, 3.17]. A few configurations were explored for the STAR detectors. Due to the importance of calibration, detailed studies of the injection line response were performed. A

description and summary of the test results and the final layout are presented in chapter 5 of this thesis.

3.3.3 Anode region

In the drift region, cathodes on the n-side surface and p-side surface are biased symmetrically. The parabolic potential generated by the cathodes keeps the electron cloud in the center plane of the detector. Close to the anodes the electron cloud has to be shifted towards the n-surface of the detector, where the anodes are placed. To shift the electron cloud, the cathodes near the anodes are gradually biased asymmetrically between the n and p sides. Cathodes on the p-side (p0 to p20) are biased more negatively than the cathodes on the n-side (n0 to n20) such that the minimum of the parabolic potential shifts towards the n-side. To avoid undesirable surface effects, the asymmetry between the two sides is kept small in the cathodes region. Typical values of the cathodes are n0=-30V and p0=-50V. The final "push" of the electron cloud towards the surface into the anodes is achieved by a potential generated using the focusing cathodes, "E1" and "W1". These electrodes are biased separately and the charge collection efficiency is greatly dependent on those biases. A top view schematic of the anode region design was shown in figure 3.6. Figure 2.8 showed a cross section view of the anode region along the drift direction.

3.3.3.1 Description of the focusing region

The anodes consist of 240 segmented $n+$ implanted squares of about $200\times200\ \mu m^2$. A $400\ \mu m$ wide $p+$ implant electrode, called "E1", surrounds each and all anodes. The gap between the anode $n+$ implant and "E1" $p+$ implants is around $11\text{-}\mu m$. The "E1-anode" structure can be considered a diode, and by biasing "E1" negatively with respect to the anodes, the diode is in a reversed bias

condition. Consequently, the Silicon underneath "E1" is depleted, thus insulating the anodes from one another. Maintaining a low level of reverse current between E1 and the anodes is important to keep the noise levels low.

"W1" is a *420 μm* wide p+ electrode placed on the p-side surface, opposite to the anodes and "E1". The combined bias of "E1" and "W1" determines the potential distribution in the anode region. Parallel to "W1", on the outer side of the detector, there are three extra cathode strips (W0, W-1 and W-2), *60 μm* wide. These electrodes are kept floating and help to decrease the bulk potential from "W1" bias value down to zero.

Back on the n-side of the detector, parallel to "E1", a thin *n+* implanted line is placed across the detector. This implanted line, called "Guard anode" is kept at ground potential to collect surface currents that were generated in the *Si-SiO_2* interface. Also, leakage currents from the cathode chain and from the high voltage guard-lines are collected by the guard anode. Therefore the current measured in the guard anode is a good parameter to monitor the detector performance. In general, this current is expected to be lower than *50 μA*.

3.3.3.2 Focusing voltages

The potential distribution in the anode region is determined mainly by the voltages applied to "E1" and "W1". These voltages should be optimized to provide a good focusing of the electrons and therefore no charge loss. To determine the ideal set of voltages, a few points must be considered.

- The focusing voltages have to be sufficiently high in order to deplete the entire thickness of the detector in that region. Electrons passing through undepleted areas are likely to recombine causing inefficiency in the charge collection. With "E1" kept at zero potential, full depletion can be accomplished with

W1=-90V. But by combining the biases of "E1" and "W1", it is possible to fully deplete the detector with much lower voltages, for example: *E1=-15V* and *W1=-30V*.

- The shape of the potential distribution has to be such that the electron cloud is "guided" into the anodes. A wrong set of bias values can create potential wells or barriers that can trap or block the electrons from reaching the anodes.

- Breakdown voltages of the "E1-anode" junction, the "E1-n0" junction and the "W1-p0" junction limit the range of acceptable voltages for "E1" and "W1". The breakdown voltages depend on the size and quality of the junction gap. The "E1-anode" junction is the most delicate junction, and was measured to breakdown for voltage differences above *50V*.

Focusing voltages were studied by measuring the anode signal as a function of "E1" and "W1" voltages. The signal was generated by a laser pulse positioned in the drift region and read out through a pre-amplifier/shaper channel. A more detailed description of the testing setup will be presented in the next chapter. Figure 3.11(a) shows a typical focusing map measured for a single anode on a STAR-2.7 detector prototype. It should be noticed that the signal amplitude is strongly dependent on the values of "E1" and "W1". Also, it was measured that the optimal focusing voltage varied from anode to anode. Therefore, for a set of focusing voltages, the charge collection varied across the detector, from anode to anode.

Figure 3.11(b) shows the simulated negative electric potential near the anode region for the STAR-2.7 detector. This potential distribution was calculated by solving numerically the Poisson equation using a simulation package [ref. 3.14]. A *3.0 kΩ·cm* Silicon substrate was considered with an interface state density of $2\times10^{11}\ cm^{-2}$. In this figure, the potential distribution shown is for the cross section plane of the detector, formed by the drift direction and the traversing

direction. It is assumed that the potential is uniform along the direction parallel to the anodes. The equipotentials on this plot are defined by the electrodes on both surfaces.

(a) Voltage focusing map **(b) Simulated potential distribution**

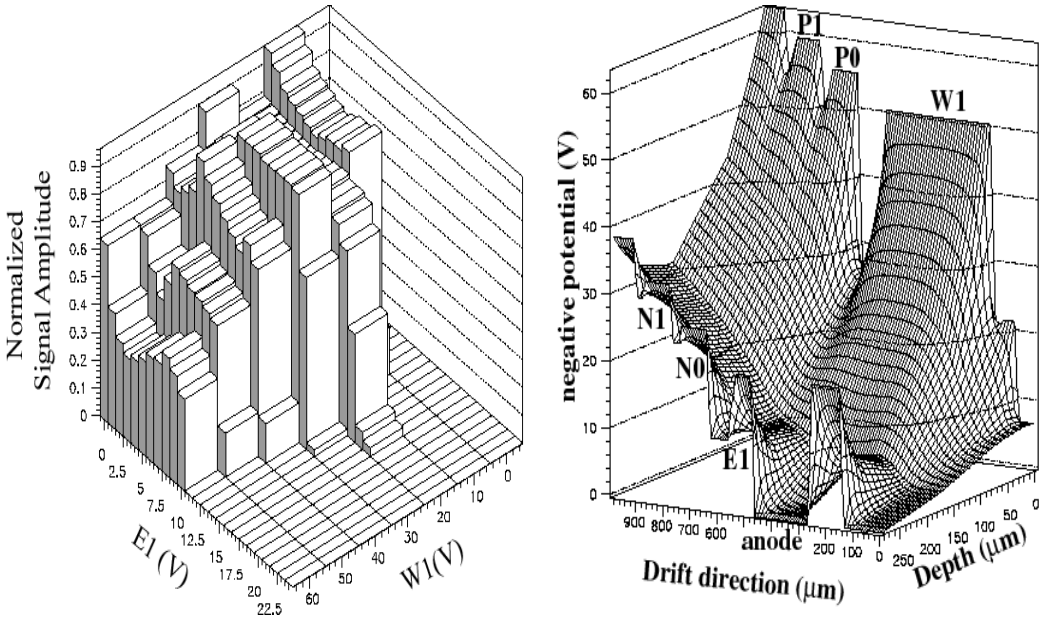

Figure 3.11: *(a) Measured signal amplitude dependence on the focusing voltages "E1" and "W1" for STAR-2.7 detectors. (b) Negative electric potential calculated for the anode region of the STAR-2.7 detector design..*

The electrode voltage values were chosen to be a typical set of biases used in the detectors. An important effect shown in this simulation is the existence of potential wells between electrodes, near the surface. This potential sag is created due to positive charges that are fixed at the *Si-SiO₂* interface. Two "deep" wells can be seen in the anode region, between the "E1" and "N0" and between "W1" and "P0". These two wells, can be a substantial potential trap for the drifting electrons, creating inefficiency in the charge collection.

3.3.3.3 Design change from STAR-2.7 to STAR-2.9

To improve the charge collection uniformity along the anodes, some changes were made in the design of the focusing region from detector prototypes STAR-2.7 to STAR-2.9. These changes were based on the focusing map results and the potential distribution simulations shown previously.

(a) Voltage focusing map **(b) Simulated potential distribution**

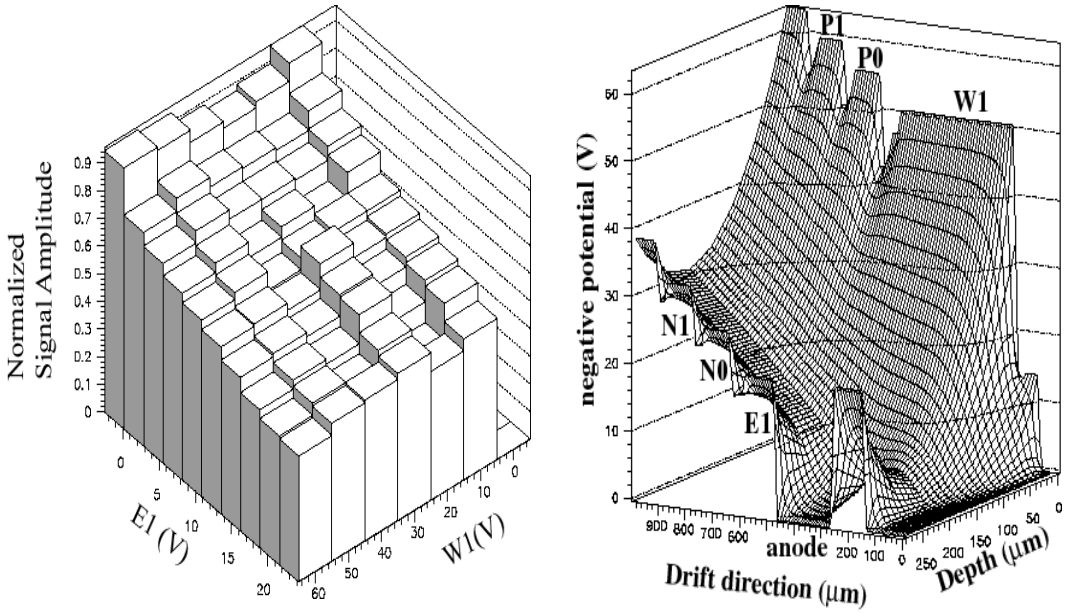

Figure 3.12: *(a) Measured signal amplitude dependence on the focusing voltages "E1" and "W1" for STAR-2.9 detectors. (b) Negative electric potential calculated for the anode region of the STAR-2.9 detector design.*

To minimize the potential wells between electrodes, the effective gaps between "E1-N0" and "W1-P0" were reduced. Figure 3.12(b) shows the results of electric potential simulation calculated for the STAR-2.9 design. The potential well between electrodes is considerably smaller compared to the results from the STAR-2.7 design.

Also, to minimize the probability of voltage breakdown between "E1" and the anodes, the gap between the n+ implant of the anodes and the p+ implant of "E1" was increased from *11 μm* to *20 μm*. This allowed to bias "E1" up to higher negative voltage values.

A typical focusing voltage map measured on a STAR-2.9 detector is shown in figure 3.12(a). It is immediately obvious that the focusing region in which a signal is measured is much broader. In addition, compared to figure 3.11, the signal amplitude is less susceptible to the different values of "E1" and "W1". Therefore, a more uniform charge collection was observed across the anodes.

3.3.4 Protection guard area

The protection guard region is composed of electric lines connected to the cathodes on both sides of the detector. The function of these guard lines is to lower the potential on the sides of the detector in a controlled manner. In addition, it connects electrically the cathodes from the opposite drift areas of the detector. To minimize the guard region the guard lines were connected only every 10 cathode strips. Figure 3.13 shows one of the edges of the detector, near the high voltage region. Each guard line is an implant of approximately *10 μm* width with a *60 μm* Aluminum overlay and a pitch between lines of *100 μm*. The guard region has a maximum voltage drop of approximately *7,000 V/cm*. This value is well below the limit for air breakdown (*30,000V/cm*).

Originally, two types of guard lines were used: p+ implanted guard lines with an Aluminum overlay, and field plate strips. The two types were tested in an earlier prototype version (STAR2.7). Early results indicated a better performance with the field plate guard lines. Due to the fact that they do not make a direct contact with the detector bulk, a higher voltage drop could be applied without generating currents. The voltage limit of the field plate guard lines is mainly

determined by the electric breakdown in the air, which occur at voltage differences above *3000 V/cm*. Results from the prototype detectors STAR2.7 produced with implanted guard lines presented a higher guard anode leakage current and a parabolic voltage distribution.

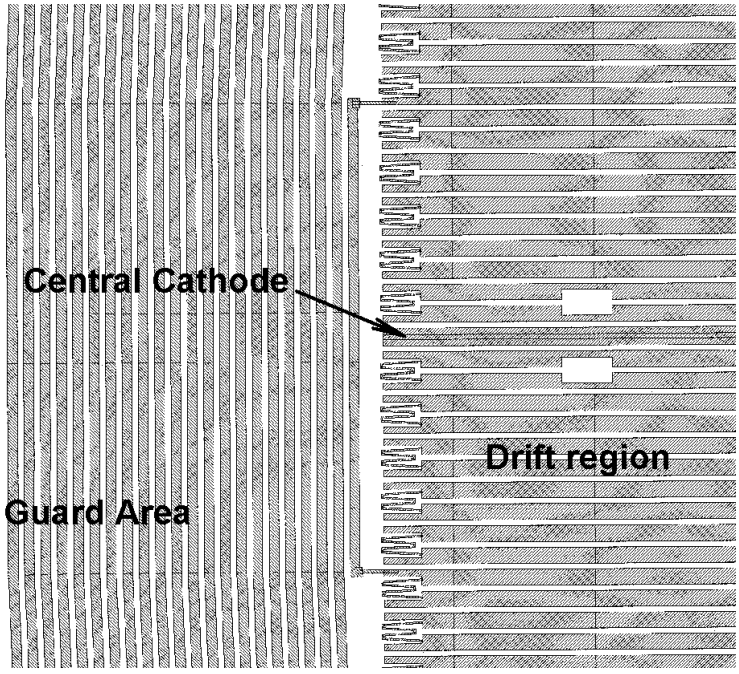

Figure 3.13: *Schematic view of the high voltage region of the detector, near the guard area, in the center of the detector.*

However, the implanted guard lines have the advantage of introducing a more precise bulk potential due to the direct connection to the bulk. In addition, they are less susceptible to external damages, such as scratches on the surface of the detector. For this reason, it was chosen to proceed with the implanted guard lines for the final detector design. The guard area was slightly increased to have a smaller field, *200 V/cm*, to avoid voltage breakdowns and leakage currents. The excellent voltage distribution and the low guard anode currents measured on detectors using the final design document the improvement of the implanted guard line structure.